ON FINITE DIFFERENCE SCHEMES FOR THE 3-D WAVE EQUATION USING NON-CARTESIAN GRIDS

Brian Hamilton
Acoustics and Audio Group
University of Edinburgh
b.hamilton-2@sms.ed.ac.uk

Stefan Bilbao
Acoustics and Audio Group
University of Edinburgh
sbilbao@staffmail.ed.ac.uk

ABSTRACT

In this paper, we investigate finite difference schemes for the 3-D wave equation using 27-point stencils on the cubic lattice, a 13-point stencil on the face-centered cubic (FCC) lattice, and a 9-point stencil on the body-centered cubic (BCC) lattice. The tiling of the wavenumber space for non-Cartesian grids is considered in order to analyse numerical dispersion. Schemes are compared for computational efficiency in terms of minimising numerical wave speed error. It is shown that the 13-point scheme on the FCC lattice is more computationally efficient than 27-point schemes on the cubic lattice when less than 8% error in the wave speed is desired.

1. INTRODUCTION

Finite difference (FD) schemes have long been used to approximate solutions to the wave equation [1, 2]. The wave equation can be used to model 3-D sound propagation in terms of pressure or velocity potential [3] and FD schemes provide an approximation to such acoustic fields. This has been used for 3-D room acoustics modelling [4], for the cavities of percussion instruments [5–7], and for artificial reverberation purposes [8, 9]. Certain FD schemes are also known by an equivalent wave-scattering formulation called the *digital waveguide mesh* (DWM) [10], which has seen much use in the acoustics and audio signal processing community [8] due to its simplicity and passive construction.

Such FD approximations are carried out on temporal and spatial grids. The spatial grid is usually the Cartesian grid (the integer or cubic lattice [11]), but non-Cartesian grids (lattices) can also be used in 3-D [11], such as the body-centered cubic (BCC) grid [12], the face-centered cubic (FCC) grid [6, 7], and the "diamond lattice" (not a lattice in the strict sense [11, 13]), which is used in the "tetrahedral DWM" [14] . Furthermore, there are many approximations to the 3-D Laplacian operator that pertain to each grid [12, 15]. Numerical dispersion in a FD scheme can give rise to audible artifacts [16, 17] and this largely depends on the choice of the spatial grid and approximation to the Laplacian. Mitigating these effects in an efficient manner is critical for large-scale 3-D room acoustics simulations since these simulations can be prohibitively expensive in terms of memory and computation time, even with the use of graphical processing units (GPUs) [18, 19]. Making sense of all these choices has been the subject of many studies [12, 20–23], however, the treatment of non-Cartesian grids has been lacking important details, as will be seen in this paper.

It has recently been shown that one must consider the cell that tiles the wavenumber space, also known as the Brillouin zone of the lattice in crystallography [13], to properly analyse numerical dispersion and computational efficiency of FD schemes on the 2-D hexagonal grid [24]. While the Brillouin zone has long been considered in multidimensional sampling on non-Cartesian grids [25], it has yet to be considered in the context of FD schemes for the 3-D wave equation. The computational efficiencies of special cases of a 27-point stencil (approximation to the Laplacian) on a cubic lattice have been studied previously [23], and while this encompassed 13-point and 9-point special cases related to the FCC and BCC lattices respectively, it will be seen that it is necessary to consider both the stencil and the lattice on which it operates.

The main contributions of this paper are to consider the wavenumber cells on non-Cartesian grids to show how it relates to stability conditions and the analysis of numerical dispersion, and to compare computational efficiencies of FD schemes in terms minimising numerical dispersion for audio and acoustics applications.

The paper is organised as follows. In Section 2, we introduce the finite difference schemes and in Section 3, we discuss the discretisation of time and space. In Section 4, we consider the tiling of the wavenumber space for non-Cartesian grids and in Section 5, stability conditions are discussed with respect to the wavenumber tilings. Numerical dispersion and computational efficiency are analysed in Sections 6 and 7 respectively. Conclusions are given in Section 8.

1.1 3-D Wave Equation

Modelling 3-D room acoustics usually begins with the 3-D wave equation:

$$\left(\frac{\partial^2}{\partial t^2} - c^2\Delta\right) u = 0\,, \quad \Delta = \frac{\partial^2}{\partial x^2} + \frac{\partial^2}{\partial y^2} + \frac{\partial^2}{\partial z^2} \quad (1)$$

where c is the wave speed, Δ is the 3-D Laplacian operator, t is time, and $u = u(t, \boldsymbol{x})$ is the solution to be approximated for $\boldsymbol{x} \in \mathbb{R}^3$ ($\boldsymbol{x} = (x, y, z)$). The variable u can

represent pressure or a velocity potential [3,20]. A room is not complete without walls but this study is only concerned with the interior (the bulk of the computation) so boundary conditions will not be considered here. At this point it is worth mentioning that the FD schemes considered in this paper are those that can be coupled to existing boundary conditions that model frequency-dependent walls [23,26].

2. FINITE DIFFERENCE SCHEMES

2.1 Time Difference Operator

In FD schemes, the variable u is replaced by an approximation to u, $\hat{u} = \hat{u}(t, \boldsymbol{x})$, and partial differential operators are replaced by finite difference operators. A standard FD approximation to $\frac{\partial^2}{\partial t^2}$ is the following:

$$\delta_{tt,k}\hat{u} = \frac{1}{k^2}(\hat{u}(t+k,\boldsymbol{x}) - 2\hat{u}(t,\boldsymbol{x}) + \hat{u}(t-k,\boldsymbol{x}))\,, \quad (2)$$

where k is the time-step, which could be chosen to be $k = 1/F_s$ where F_s is an audio sampling rate like 44.1 kHz.

2.2 Finite Difference Approximations to the Laplacian

Approximations to the 3-D Laplacian can be built using the following FD operator:

$$\delta_{\Delta,\Omega,h}\hat{u} = \frac{\kappa}{h^2}\sum_{i=1}^{|\Omega|}(\hat{u}(t,\boldsymbol{x}+\boldsymbol{v}_i h) - 2\hat{u}(t,\boldsymbol{x}) + \hat{u}(t,\boldsymbol{x}-\boldsymbol{v}_i h))\,, \quad (3)$$

where $\Omega \subset \mathbb{R}^3$ is a set of equal-norm vectors $\boldsymbol{v}_i \in \Omega$, and $|\Omega|$ denotes the cardinality of that set. The constant h is the spatial step, which will be chosen based on the time-step and stability constraints of the FD scheme. The FD operator in (3) becomes a $(2|\Omega|+1)$-point second-order accurate approximation to the Laplacian (we also call this a *discrete Laplacian* or a *stencil*) for particular choices of Ω and κ. The standard 7-point stencil uses the standard unit vectors $\Omega_C = \{\hat{\boldsymbol{e}}_x, \hat{\boldsymbol{e}}_y, \hat{\boldsymbol{e}}_z\}$. We also consider a 13-point stencil that uses the following six vectors from the FCC lattice: $\Omega_F = \{\hat{\boldsymbol{e}}_x \pm \hat{\boldsymbol{e}}_y, \hat{\boldsymbol{e}}_x \pm \hat{\boldsymbol{e}}_z, \hat{\boldsymbol{e}}_y \pm \hat{\boldsymbol{e}}_z\}/\sqrt{2}$, and a 9-point stencil that uses the following four vectors from the BCC lattice: $\Omega_B = \{\hat{\boldsymbol{e}}_x \pm \hat{\boldsymbol{e}}_y \pm \hat{\boldsymbol{e}}_z, \hat{\boldsymbol{e}}_x \mp \hat{\boldsymbol{e}}_y \pm \hat{\boldsymbol{e}}_z\}/\sqrt{3}$. These stencils are shown in Fig. 1. For these choices of Ω we get the following condition for consistency:

$$\kappa = \frac{3}{|\Omega|\|\boldsymbol{v}\|^2}\,, \quad (4)$$

where $\|\boldsymbol{v}\|$ denotes the Euclidean norm of any $\boldsymbol{v} \in \Omega$.

We can also build a consistent approximation to the Laplacian as a weighted combination of these stencils:

$$\delta_{\boldsymbol{\Delta},\boldsymbol{\alpha},\Upsilon,h}\hat{u} = \sum_{j=1}^{|\Upsilon|}\alpha_j\delta_{\Delta,\Omega_j,h}\hat{u}\,, \quad \sum_{j=1}^{|\Upsilon|}\alpha_j = 1\,, \quad (5)$$

where Υ is a set of sets and $\boldsymbol{\alpha} = (\alpha_1, \ldots, \alpha_{|\Upsilon|})$. In this study, we consider $\Upsilon_F = \{\Omega_F\}$, $\Upsilon_B = \{\Omega_B\}$, and a 27-point stencil with $\Upsilon_C = \{\Omega_C, \sqrt{2}\Omega_F, \sqrt{3}\Omega_B\}$.

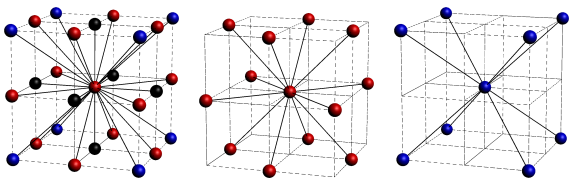

(a) Cubic (b) FCC (c) BCC

Figure 1: Some spatial points in the cubic lattice and scaled FCC and BCC lattices. Lines from center point denote vectors of associated stencils. The 27-point stencil $\delta_{\boldsymbol{\Delta},\boldsymbol{\alpha},\Upsilon_C,h}$ uses all the points in (a), whereas the 7-point stencil $\delta_{\Delta,\Omega_C,h}$ uses the black points and the center point.

2.3 Finite Difference Scheme for Wave Equation

Combining these operators we have a FD scheme for the 3-D wave equation:

$$\left(\delta_{tt} - c^2\delta_{\boldsymbol{\Delta},\boldsymbol{\alpha},\Upsilon,h}\right)\hat{u} = 0\,, \quad (6)$$

which is updated in time with the explicit recursion:

$$\hat{u}(t+k,\boldsymbol{x}) = (c^2k^2\delta_{\boldsymbol{\Delta},\boldsymbol{\alpha},\Upsilon,h} + 2)\hat{u}(t,\boldsymbol{x}) - \hat{u}(t-k,\boldsymbol{x})\,, \quad (7)$$

given some initial conditions.

3. DISCRETISING TIME AND SPACE

In practice, the FD approximation is calculated at a countable set of points in space and time, denoted by a lattice (a grid of points). The temporal grid is simply the integer lattice $\mathbb{Z}$ scaled by the time-step k:

$$\boldsymbol{T}_k = \{t_n = nk, n \in \mathbb{Z}\}\,. \quad (8)$$

A spatial lattice in 3-D is defined by:

$$\boldsymbol{G}_h = \{\boldsymbol{x}_{\boldsymbol{m},h} = \boldsymbol{m}^T\boldsymbol{V}h \in \mathbb{R}^3\,, \boldsymbol{m} \in \mathbb{Z}^3\}\,, \quad (9)$$

where $\boldsymbol{V}$ is a *generator matrix* [11] made up of any three column vectors chosen from Ω_C, Ω_F, and Ω_B for the cubic, FCC, and BCC lattices respectively. The approximated solution will have a certain bandwidth (spatial and temporal) given some time-step k, grid spacing h (spatial step), and discrete Laplacian $\delta_{\boldsymbol{\Delta},\boldsymbol{\alpha},\Upsilon,h}$. Given the bandwidth in the approximation, there will be a temporal and spatial lattice on which values of $\hat{u}(t,\boldsymbol{x})$ will have to be calculated so that the *continuous approximation* $\hat{u}(t,\boldsymbol{x})$ can be completely reconstructed [25]. For this reason, we only need to compute $\hat{u}(t,\boldsymbol{x})$ on a spatial and temporal grid, i.e., we calculate the set: $\{\hat{u}(t,\boldsymbol{x}) : t \in \boldsymbol{T}_k, \boldsymbol{x} \in \boldsymbol{G}_h\}$, where $\boldsymbol{T}_k$ and $\boldsymbol{G}_h$ are the appropriate grids for our FD scheme.

Choosing the appropriate grid for a given stencil is not always obvious and one must be careful so that only necessary values of $\hat{u}(t,\boldsymbol{x})$ are computed. For example, consider the FD scheme (6) with the 27-point stencil ($\Upsilon = \Upsilon_c$). Two special cases, among others, were analysed in a study on the computational efficiency of this scheme when employed on the cubic lattice: the *close-cubic packed* (CCP) scheme ($\boldsymbol{\alpha} = (0,1,0)$), and the *octahedral* scheme ($\boldsymbol{\alpha} =$

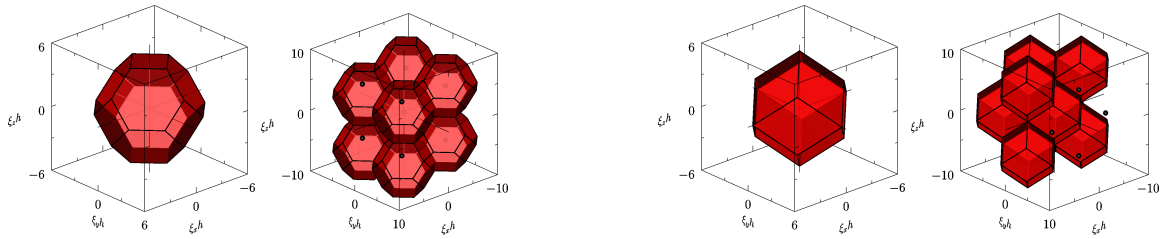

(a) FCC (b) BCC

Figure 2: Wavenumber cells, wavenumber tilings, and dual lattices (black dots) of FCC and BCC lattices.

$(0, 0, 1)$) [23]. As can be deduced from Fig. 1, the cubic lattice can be constructed with two scaled [1] and interleaved FCC lattices [11]. Note that the red points in Fig. 1(a) are part of one FCC lattice, and the blue and black points are part of another, shifted FCC lattice. As a consequence, the FD scheme with $\boldsymbol{\alpha} = (0, 1, 0)$ operates on two *disjoint* sets of points, each pertaining to one FCC lattice; this results in two *decoupled* schemes on FCC subgrids. [2] When such a scheme is employed on the cubic lattice, the FD approximation on half of the spatial points provides no additional information (bandwidth) that cannot be reconstructed from the values of $\hat{u}(t, \boldsymbol{x})$ on one FCC lattice. As such, the appropriate lattice for the CCP scheme is the FCC lattice. Similarly, the cubic lattice can be constructed from four scaled and interleaved BCC lattices [11], so, for the same reasons, the appropriate lattice for the octahedral scheme is a single BCC lattice. These features were not considered in [23], so we can improve on the reported computational efficiency, which depends on density of the spatial lattice, if we choose the appropriate lattices, as will be seen later.

4. TILING THE WAVENUMBER SPACE

It is well known that the Fourier transform of a discrete signal is periodic with period $2\pi/k$, where k is the sampling period, or time-step. The same applies to discrete multidimensional signals on spatial lattices, but the periodicity of the spatial frequencies, or wavenumbers $\boldsymbol{\xi} = (\xi_x, \xi_y, \xi_z) \in \mathbb{R}^3$, is more subtle. In general, the periodicity represents a regular tiling of the continuous frequency space which is given by the Voronoi tessellation of the *dual lattice*. The dual lattice has the generator matrix $(\boldsymbol{V}^{-1})^T$ when $\boldsymbol{V}$ is the generator matrix of the *direct lattice* and consists of unit-norm vectors [11]. The dual lattice is further scaled by 2π and the inverse of the time or spatial period [13]. This leads to the well-known sampling theorem in 1-D and this was extended to sampling in multiple dimensions [25]. The cell that makes up the tiling of the wavenumber space is known as the *Brillouin zone* of the direct lattice in crystallography [13] and the *wavenumber cell* of the lattice in the context of multidimensional sampling [25]. The cubic lattice is self-dual [11], so the wavenumber tiling is composed of cubic wavenumber cells with sides of length $2\pi/h$. Previous studies have assumed a cubic wavenumber cell for FD schemes for the 3-D wave equation on the FCC and BCC lattices, but this is not the case. The FCC and BCC lattices form a dual pair [11] and their wavenumber cells are the truncated octahedron and the rhombic dodecahedron respectively [11, 13]. These cells and their tilings are shown in Fig. 2.

We can determine how well a set of values on a spatial lattice can reconstruct an isotropic spatial signal (bandwidth cuts off at the same $|\boldsymbol{\xi}|$ in all directions) from the dual lattice and its associated wavenumber tiling [25]; this is called the *sampling efficiency* of the lattice. Some studies have chosen specific lattices for FD schemes solely based on sampling efficiency [28–30], but this can be misleading. Sampling efficiency is not a suitable metric in choosing a grid for a FD scheme because, aside from at the initial conditions, sampling is not part of the FD approximation. The solution $u(t, \boldsymbol{x})$ is unknown so it cannot be sampled (aside from the special case in 1-D [16]); it must be approximated by $\hat{u}(t, \boldsymbol{x})$ at points on a grid and the rest of $\hat{u}(t, \boldsymbol{x})$ can be reconstructed using multidimensional sinc interpolation. The efficiency in computing an accurate FD approximation depends on other factors besides the lattice on which it is employed, such as the stencil used, the combined density of the spatial and temporal grid set according to stability constraints, the number of arithmetic operations at each update, and most importantly, the particular metric used to measure efficiency, which could be in terms of order of accuracy given by a Taylor expansion or accuracy in the numerical wave speed.

We argue that the key to choosing a lattice is its rotational symmetry, which is related to the *kissing number* problem (how many non-overlapping spheres can touch or *kiss* a central sphere of the same size) [11]. We are essentially using points on the spatial lattice to approximate an isotropic (directionally-independent) operator, the Laplacian, so symmetry in the lattice plays a large role in emulating this isotropy. For example, two shells of points are required for an isotropic stencil (to the fourth-order error term) on the 2-D square lattice [31], but the lattice with the highest kissing number in 2-D, the hexagonal lattice, provides an isotropic stencil using only the first shell of points [31].

The lattice in 3-D with the highest kissing number and the most symmetry is the FCC lattice [11]. The 13-point stencil from the FCC lattice is not quite isotropic, but it has been observed that it is *nearly isotropic* [22, 23]. This can be seen in Fig. 3, where isosurfaces (surface of equal error, as a function of $\boldsymbol{\xi}$) of the second-order error terms in approximations to the Laplacian are shown. Among the

[1] We use the term "scaled" when a lattice generated with unit-norm vectors is multiplied by something other than the grid spacing h.

[2] The same observation has been made in the context of lattice Boltzmann simulations [27].

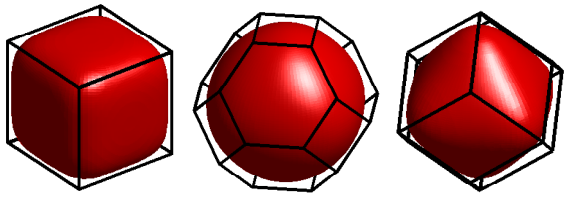

(a) 7-point stencil (b) 13-point stencil (c) 9-point stencil

Figure 3: Equal isosurfaces of first error-term in Taylor expansions of Fourier symbols of approximations to Laplacian. Isotropic error gives a sphere.

three isosurfaces displayed in Fig. 3 the isosurface pertaining to the 13-point FCC stencil is the closest to a sphere (isotropic). We also observe that they loosely conform to the wavenumber cells of their associated lattices. A rounder wavenumber cell is more amenable to an isotropic error since the full error must ultimately conform to the tiling of the wavenumber space.

Considering that the Fourier symbol of the Laplacian describes concentric spherical shells (isosurfaces of scalar values), we can take another point of view: in essence, we are trying to fit a sphere into the wavenumber cell. Thus, we require the roundest wavenumber cell. This problem could be formulated as finding the lattice whose wavenumber cell has a ratio of *inradius* (largest radius for a sphere contained by the cell) to *circumradius* (the smallest radius for a sphere that contains the cell) closest to unity (this ratio for a sphere). This is a combination of the kissing problem (maximise inradius) and the *covering problem* (what is the least dense arrangement of overlapping spheres that covers space; minimise circumradius) [11]. These ratios are approximately 1.29, 1.41, and 1.73 for the FCC, BCC, and cubic lattices respectively. This is similar, but different from finding the optimal sampling lattice for an isotropic signal, which is essentially the sphere packing problem in the wavenumber space [25], and for lattices, the kissing number problem [11]. The 2-D hexagonal lattice is self-dual, and solves both the kissing number problem and the covering problem, so sampling arguments [28], while unfounded, arrive at the same conclusion. This line of reasoning has also been used in 3-D to select the BCC lattice [29], which is optimal for sampling because its dual, the FCC lattice, is the lattice with the highest kissing number and sphere packing density [25]. However, it will be seen that the BCC lattice is not ideal in the context of FD schemes for the 3-D wave equation. It is interesting to note that a recent study also followed sampling arguments [30], but arrived at the FCC lattice by conflating the optimal sampling lattice with its dual.

5. STABILITY

Using von Neumann's method for determining stability conditions in FD schemes [32], it is sufficient to consider a plane wave of the form: $\hat{u}(t,\boldsymbol{x}) = e^{\jmath(\omega t + \boldsymbol{\xi}\cdot\boldsymbol{x})}$, where ω is the temporal frequency and $(\omega,\boldsymbol{\xi}) \in \mathbb{R}^4$. It helps to define a normalised wavenumber $\boldsymbol{\xi}_h = \boldsymbol{\xi}h$ and normalised frequency $\omega_k = \omega k$. Inserting the plane wave into the FD

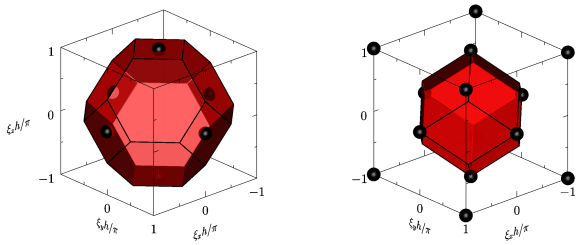

(a) FCC (b) BCC

Figure 4: Scaled FCC and BCC wavenumber cells inscribed in cubic wavenumber cell. Arguments of the maxima in $|\mathcal{D}_{\Delta,\sqrt{2}\Omega_F,h}|$ and $|\mathcal{D}_{\Delta,\sqrt{3}\Omega_B,h}|$ denoted by black spheres.

scheme then gives a dispersion relation of the form:

$$\mathcal{D}_{tt}(\omega_k) = \lambda^2 \mathcal{D}_{\boldsymbol{\Delta},\boldsymbol{\alpha},\Upsilon}(\boldsymbol{\xi}_h)\,, \tag{10}$$

where $\lambda = ck/h$ is the Courant number and

$$\mathcal{D}_{tt}(\omega_k) = -4\sin^2(\omega_k/2)\,, \tag{11}$$

$$\mathcal{D}_{\boldsymbol{\Delta},\boldsymbol{\alpha},\Upsilon}(\boldsymbol{\xi}_h) = -4\sum_{j=1}^{|\Upsilon|}\alpha_j\kappa_j\sum_{i=1}^{|\Omega_j|}\sin^2(\boldsymbol{\xi}_h\cdot\boldsymbol{v}_{j,i}/2) \tag{12}$$

for $\boldsymbol{v}_{j,i} \in \Omega_j$. The scheme is stable if we can ensure that no real wavenumbers produce growing solutions in time. This requires finding a maximum for $|\mathcal{D}_{\boldsymbol{\Delta},\boldsymbol{\alpha},\Upsilon}(\boldsymbol{\xi}_h)|$ and we get the following stability condition:

$$\lambda \leq \lambda_{\max,\boldsymbol{\alpha}} = \sqrt{\frac{4}{\max_{\boldsymbol{\xi}_h}|\mathcal{D}_{\boldsymbol{\Delta},\boldsymbol{\alpha},\Upsilon}(\boldsymbol{\xi}_h)|}} \tag{13}$$

In deriving this condition we have not specified a grid, but $\mathcal{D}_{\boldsymbol{\Delta},\boldsymbol{\alpha},\Upsilon}(\boldsymbol{\xi}_h)$ is periodic according to the wavenumber tiling of the appropriate grid for the stencil. It is then sufficient to consider just one wavenumber cell of the appropriate lattice. So in the CCP and octahedral schemes on cubic lattices, the stability condition is found within the wavenumber cell of scaled FCC and BCC lattices respectively, but an exhaustive search over a larger domain will also locate the maximum. For the schemes considered here, $|\mathcal{D}_{\boldsymbol{\Delta},\boldsymbol{\alpha},\Upsilon,h}(\boldsymbol{\xi})|$ is *multilinear* in $\cos(\xi_x h)$, $\cos(\xi_y h)$, and $\cos(\xi_z h)$ variables, and it can be shown that the maximum occurs at either the faces, center of edges, or vertices of a cubic wavenumber cell [12]. As we can see in Fig. 4, the wavenumber cells of the scaled FCC and BCC lattices are neatly inscribed in a cube with sides of $2\pi/h$. The points where the maximum of $|\mathcal{D}_{\Delta,\sqrt{2}\Omega_F,h}|$ occurs line up with the square faces of the truncated octahedron wavenumber cell for the CCP scheme. Similarly, the points where the maximum of $|\mathcal{D}_{\Delta,\sqrt{3}\Omega_B,h}|$ occurs line up with vertices of the rhombic dodecahedron wavenumber cell for the octahedral scheme (the corners of the cube pertain to vertices of replicated dodecahedral cells).

It has been shown that the stability conditions for the 27-point stencil scheme are [12]:

$$-2\alpha_1 \leq \alpha_2 \leq 2\alpha_1 + 1\,, \tag{14}$$

$$\lambda \leq \lambda_{\max,\boldsymbol{\alpha}} = \min\left(1, \frac{1}{\sqrt{2\alpha_1+\alpha_2}}, \frac{1}{\sqrt{2\alpha_1-\alpha_2+1}}\right), \tag{15}$$

and from (15) we can get the stability conditions for the 13-point and 9-point FD schemes after we rescale the grid spacings. For the 13-point ($\Upsilon = \Upsilon_F$) and 9-point ($\Upsilon = \Upsilon_B$) schemes we have the respective stability conditions:

$$\lambda \leq \sqrt{1/2}\,, \quad \lambda \leq \sqrt{1/3}\,. \tag{16}$$

Note that the condition for the 13-point scheme is different from the Courant number used in the "dodecahedral DWM" [6], which means this case was not covered in a study comparing DWM topologies [22]. It was observed that the dodecahedral DWM had good numerical dispersion properties [22] and since numerical dispersion is minimised when the Courant number is set to $\lambda_{\max,\boldsymbol{\alpha}}$ [16] the FD scheme on the FCC lattice will provide less dispersion. [3]

6. NUMERICAL DISPERSION

Inserting the plane wave $u(t,\boldsymbol{x}) = e^{j(\omega t+\boldsymbol{\xi}\cdot\boldsymbol{x})}$ into the wave equation we get the dispersion relation $\omega^2 = c^2|\boldsymbol{\xi}|^2$, which tells us that the *phase velocity* ($\omega(\boldsymbol{\xi})/|\boldsymbol{\xi}|$) of each plane wave is the wave speed c. However, in the FD scheme the relationship is not linear and we get a frequency- and direction-dependent wave speed in the approximation $\hat{u}(t,\boldsymbol{x})$. The *relative phase velocity* (we will just call this the *numerical wave speed*) is:

$$\hat{\nu}(\boldsymbol{\xi}_h) = \frac{\omega_k(\boldsymbol{\xi}_h)}{\lambda|\boldsymbol{\xi}_h|}\,, \quad \omega_k(\boldsymbol{\xi}_h) = \mathcal{D}_{tt}^{-1}(\lambda^2\mathcal{D}_{\boldsymbol{\Delta},\boldsymbol{\alpha},\Upsilon}(\boldsymbol{\xi}_h)) \tag{17}$$

for $\omega_k \in (0,\pi]$ and $\boldsymbol{\xi}_h \in \mathbb{B}$, where $\mathbb{B}$ is the wavenumber cell of the grid. The wave speed error, defined as $|1-\hat{\nu}(\boldsymbol{\xi}_h)|$, is the main concern in audio and acoustics applications of FD schemes. Higher frequencies tend to travel slower and this causes transients to be smeared over space and time. It is therefore of interest to analyse numerical dispersion in such schemes, but a proper analysis of the wave speed error requires the correct wavenumber cell on non-Cartesian grids.

With 2-D schemes one can plot the wave speed error over the entire domain using a single contour plot [12, 24], but this is not possible for 3-D. Some possibilities to visualise the wave speed error include fixing two angles and plotting the error as a function of $|\boldsymbol{\xi}_h|$ [23]; fixing $|\boldsymbol{\xi}_h|$ and plotting the error as a function of two angles as a mapping of colours on a spherical shell [12, 22] or where the error denotes a polar radius [33]; plotting contours of two-dimensional slices of $\mathbb{B}$ [12, 23]; or fixing some error and plotting this as a three-dimensional isosurface of wavenumbers. In each of these representations one can encounter aliased wavenumbers if one does not consider the correct domain $\mathbb{B}$. If one assumes a cubic wavenumber cell for the 13- and 9-point schemes, as has been done in the past, the cell will contain aliased wavenumbers, as can be deduced from Fig. 4, or missing wavenumbers. [4] This can result in an incorrect numerical wave speed if the denominator in (17) is not adjusted accordingly to reflect the tiling of the wavenumber space.

Table 1 lists the parameters of the schemes analysed here, along with some acronyms sometimes employed in the literature [22, 23]. These acronyms stand for the standard leapfrog (SLF), interpolated wideband (IWB), interpolated isotropic (IISO2), [5] close-cubic packed (CCP), and octahedral (OCTA) schemes. The 27-point IWB and IISO2 schemes are analysed because they were identified as being the most effective 27-point schemes at reducing wave speed error [23]. Note that the CCP and OCTA schemes are analysed here on their native lattices for the reasons stated in Section 2.3, so we will refer to these as the "FCC scheme" and the "BCC scheme".

The density of a spatial grid is μ/h^3, where μ is the density of the unscaled lattice (unit grid spacing). The *computational density* (updates per unit time and space) of a scheme is then $\mu(h^3k)^{-1}$. Fixing the Courant number at the stability limit, we can write the computational density as $(c\mu/\lambda)h^{-4}$. Thus, to put schemes on an equal footing we use the spatial step $h = \sqrt[4]{\mu/\lambda}h'$ so that each scheme has the density ch'^{-4}. Similarly, we can write the computational density as $(\mu\lambda^3/c^2)k^{-4}$, so we can equalise the schemes by choosing the time-step as $k = \sqrt[4]{\mu\lambda^3}k'$. The parameter μ and the values μ/λ and $\mu\lambda^3$ for each scheme are listed in Table 1. We can now compare schemes on different grids and with different Courant numbers in terms of normalised wavenumbers $\boldsymbol{\xi}_{h'} = \boldsymbol{\xi}h'$ or normalised frequencies $\omega_{k'} = \omega k'$ by keeping h' or k' constant across all schemes.

The computational density is a metric for efficiency that has been used in previous comparisons [23] and is mostly a starting point to compare computational costs. It does not take into account specific operations like multiplications, additions, and memory reads, although these are simply an extra scaling factor. Ideally, such comparisons should be conducted in practice on specific computational hardware (see [34]).

In Fig. 5, we show isosurfaces of the 10% wave speed error, as a function of $\boldsymbol{\xi}_{h'}$. The surface displayed represents wavenumbers with 10% wave speed error, and since the wave speed error is monotonic in these schemes, any wavenumber inside the surface results in less than 10% error. These plots are normalised for computational density, but it is difficult to compare them since the wavenumber cells differ. However, it can be observed that the FCC scheme's isosurface (Fig. 5(d)) fills its wavenumber cell better than the other schemes fill their respective cells.

In Fig. 6, we show error surfaces where $|\boldsymbol{\xi}_{h'}|$ is fixed at $\pi/10$. We note that the relative comparison of Fig. 5(a) to Fig. 5(d) is more favourable to the FCC scheme than what is found in [30]. This is because we have also normalised for computations per unit time, but also because there is a mistake in the spatial density of the FCC lattice in [30].

[3] The dodecahedral DWM is left out for brevity, but a similar comparison can be found for 7-point FD scheme on the 2-D hexagonal grid and the "triangular DWM" [24].

[4] The wavenumber cells extend beyond the cube in Fig. 4 when the FCC and BCC lattices are not scaled.

[5] The second of three isotropic schemes that were examined in [23].

Table 1: Parameters for various schemes

Subfigure	lattice	# of points	Υ	$\boldsymbol{\alpha}$	μ	λ	μ/λ	$\mu\lambda^3$	Acronyms from [23]
(a)	cubic	7	Υ_C	$(1,0,0)$	1	$\sqrt{1/3}$	1.73	0.19	SLF
(b)	cubic	27	Υ_C	$(1/4,1/2,1/4)$	1	1	1.00	1.00	IWB
(c)	cubic	27	Υ_C	$(5/12,1/2,1/12)$	1	$\sqrt{3/4}$	1.15	0.65	IISO2
(d)	FCC	13	Υ_F	1	$\sqrt{2}$	$\sqrt{1/2}$	2.00	0.50	CCP*
(e)	BCC	9	Υ_B	1	$3\sqrt{3}/4$	$\sqrt{1/3}$	2.25	0.25	OCTA*

*These schemes are employed on the cubic lattice in [23] so μ and λ would change to $\mu = 1$ and $\lambda = 1$.

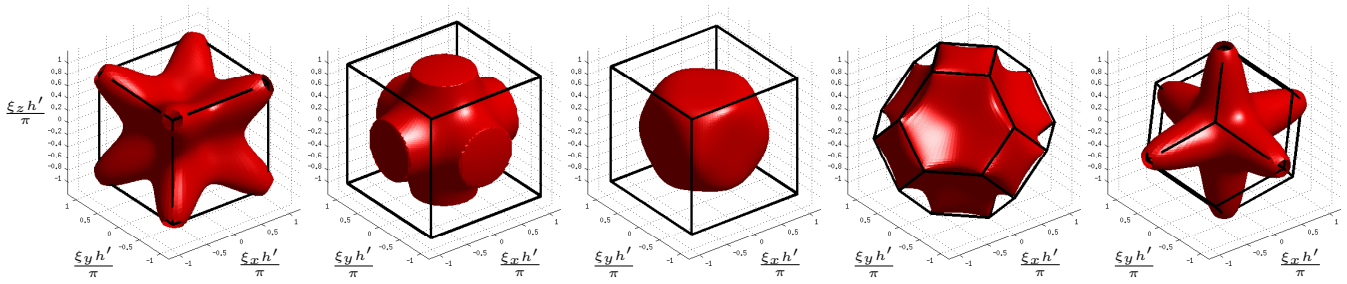

(a) SLF (b) IWB (c) IISO2 (d) FCC (e) BCC

Figure 5: 10% wave speed error isosurfaces.

From these plots we see that the FCC scheme has the lowest amount of error (for $|\boldsymbol{\xi}_{h'}| = \pi/10$).

In Fig. 7, we display volumetric slices of the wave speed error for specific planes. In these plots we can see that most of the error in the FCC scheme is less than 15%. The cubic schemes have large error near the face centers or corners of the cubic wavenumber cell. On the other hand, these wavenumbers are not represented on the scaled FCC lattice. The BCC scheme also has pronounced error near the diagonal vertices (those with a vertex figure consisting of three rhombi). The FCC scheme exhibits no numerical dispersion along the x,y, and z directions, similar to the IWB scheme; this is a useful feature for simulating axial room modes [23].

In Fig. 8, we have taken the same slices and reassigned the wave speed error to temporal frequencies ω_k and a fixed angle of propagation (polar angle) using the function $\omega_k(\boldsymbol{\xi}_h)$ in (10) [35]. We only show quadrants since these plots have four-fold symmetry. We have not normalised densities in Fig. 8 to show directionally dependent *cutoff frequencies*, of interest for audio applications. To generate Figs. 8(d) and 8(e) it is necessary to consider the correct wavenumber cell.

Finally in Fig. 9, we plot the wave speed error along the worst-case direction for each scheme as a function of normalised wavenumber $|\boldsymbol{\xi}_{h'}|$ and as a function of normalised frequency $\omega_{k'}$. Notice that the FCC scheme has slightly less dispersion than the IISO2 and IWB schemes until about 8% error. This gap will become more pronounced once we compare computational efficiencies.

7. COMPUTATIONAL EFFICIENCY

We use the relative efficiency measure introduced in [35] and employed in [23] to compare 3-D schemes for their computational efficiency in terms of minimising numerical dispersion. The basic idea is to determine how much one must increase the computational density (by reducing h or k; density scales to the fourth power) in a reference scheme (in this case, the SLF scheme) to maintain the wave speed error below some threshold in every direction. This is completely determined by the parameters in Table 1 and (17) if we increase the computational density by reducing h.[6] We plot these relative efficiencies in Fig. 10. It can be seen that if less than 8% wave speed error is desired up to some critical frequency, the FCC scheme has the best computational efficiency (using this particular metric), followed by the IISO2 and IWB schemes. If greater than 8% wave speed error is acceptable, the IWB scheme will have a smaller computational density. The data in Fig. 10 agree with the numbers reported in [23] after adjusting for the grid densities of the CCP and OCTA schemes. As such, the reported efficiencies for the CCP and OCTA schemes have been improved by a factors of two and four respectively. Nonetheless, the efficiency of the FD scheme on the BCC lattice is poor, which confirms our discussion about choosing a lattice based on sampling efficiency.

We have not taken into account the number of specific operations for each scheme and, as mentioned previously, we have left this out for brevity. However, we should point out that the FCC scheme employs less than half the neighbouring points of the 27-point stencil, so if one considers additions and memory bandwidth the FCC scheme is the most efficient scheme in a wider range of errors. Furthermore, the gap in Fig. 10 between the FCC scheme and 27-point schemes for less than 8% wave speed error increases by a factor of two. These implementation-specific details are further investigated in another study [34].

[6] This has previously been done by solving for $\boldsymbol{\xi}_h(\omega_k)$ using (10) and increasing the computational density by reducing k [23, 35], but the choice is immaterial because the measure is ultimately independent of h and k, which is apparent from the axes in Fig. 10.

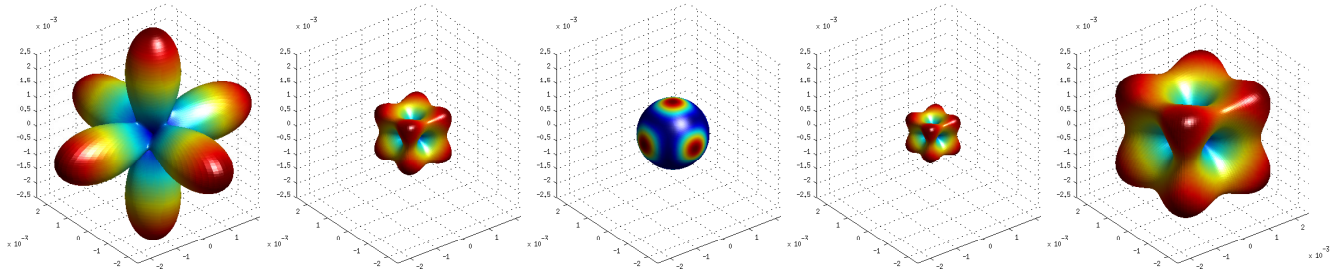

(a) SLF (b) IWB (c) IISO2 (d) FCC (e) BCC

Figure 6: Wave speed error surface for $|\boldsymbol{\xi}_{h'}| = \pi/10$. Colour mapping is relative to each plot to show detail.

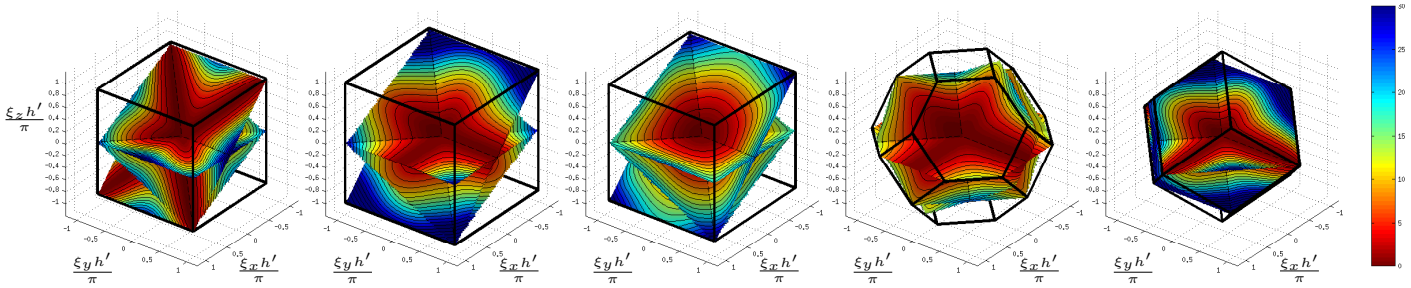

(a) SLF (b) IWB (c) IISO2 (d) FCC (e) BCC

Figure 7: Volumetric slices of wave speed error along three planes. 2% error contours.

8. CONCLUSIONS

In this paper, we have considered the wavenumber cell of non-Cartesian grids in order to compare 27-point FD schemes on the cubic lattice with a 13-point scheme on the FCC lattice and a 9-point scheme on the BCC lattice. These FD schemes have been compared in terms of numerical dispersion and using a metric of computational efficiency for minimising wave speed error. It has been shown that the 13-point scheme on the FCC lattice is the most computationally efficient scheme when less than 8% wave speed error in the approximated solution is desired up to some critical frequency. The demonstrated inefficiency of the BCC scheme confirms that sampling-based arguments are not suitable for FD schemes.

In future work, perceptual tests will be conducted to determine critical thresholds of wave speed error for the purposes of large-scale 3-D room acoustics simulations and artificial reverberation (some preliminary work can be found in [17]).

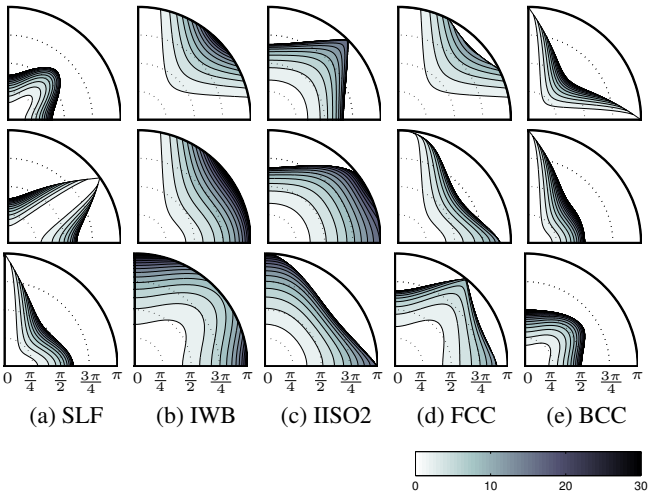

(a) SLF (b) IWB (c) IISO2 (d) FCC (e) BCC

Figure 8: Volumetric slices of wave speed error as a function of polar angle $\theta \in [0, \pi/2]$ on a plane and radius $\omega_k \in (0, \pi]$ with 2% error contours. First row: $\xi_z = 0$ plane, second row: $\xi_x = \xi_z$ plane, third row: the plane described by the zero point and the normal vector $\hat{\boldsymbol{n}} = (1, 1, 1)$.

Acknowledgments

This work was supported by the European Research Council, under grant StG-2011-279068-NESS, and by the Natural Sciences and Engineering Research Council of Canada.

9. REFERENCES

[1] R. Courant, K. Friedrichs, and H. Lewy, "Über die partiellen differenzengleichungen der mathematischen physik," *Mathematische Annalen*, vol. 100, no. 1, pp. 32–74, 1928.

[2] G. E. Forsythe and W. R. Wasow, *Finite-difference methods for partial differential equations*. New York: Wiley, 1960.

[3] P. M. Morse and K. U. Ingard, *Theoretical acoustics*. Princeton University Press, 1968.

[4] L. Savioja, T. J. Rinne, and T. Takala, "Simulation of room acoustics with a 3-D finite difference mesh," in *Proc. Int. Computer Music Conf. (ICMC)*, Danish Institute of Electroacoustic Music, Denmark, 1994, pp. 463–466.

[5] L. Rhaouti, A. Chaigne, and P. Joly, "Time-domain modeling and numerical simulation of a kettledrum," *J. Acoustical Society of America*, vol. 105, p. 3545, 1999.

[6] J. A. Laird, "The physical modelling of drums using digital waveguides," Ph.D. thesis, University of Bristol, 2001.

[7] M.-L. Aird, "Musical instrument modelling using digital waveguides," Ph.D. thesis, University of Bath, 2002.

[8] D. T. Murphy, A. Kelloniemi, J. Mullen, and S. Shelley, "Acoustic modeling using the digital waveguide mesh," *IEEE*

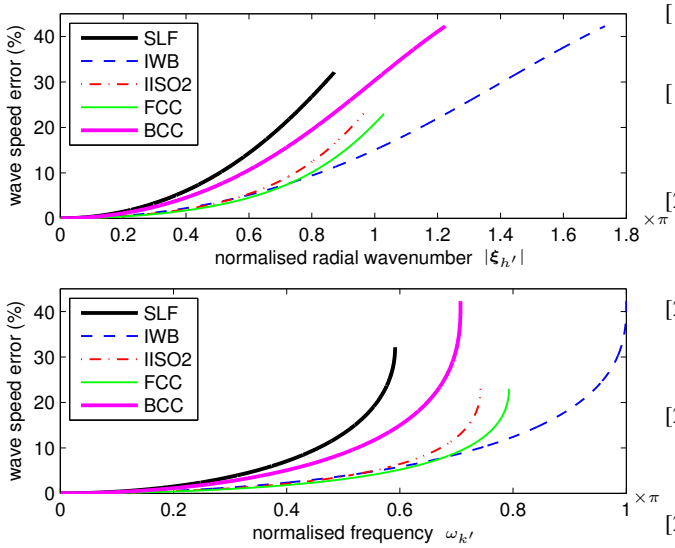

Figure 9: Wave speed error along worst-case direction for each scheme.

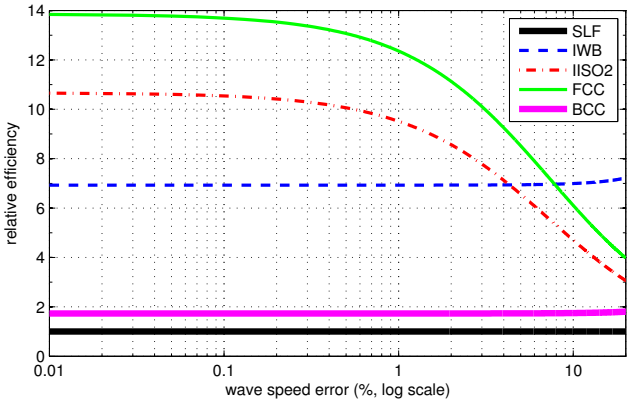

Figure 10: Efficiency for FD schemes relative to SLF.

Sig. Proc. Magazine, vol. 24, no. 2, pp. 55–66, 2007.

[9] V. Valimaki, J. D. Parker, L. Savioja, J. O. Smith, and J. S. Abel, "Fifty years of artificial reverberation," *IEEE Trans. Audio, Speech, and Language Processing*, vol. 20, no. 5, pp. 1421–1448, 2012.

[10] S. A. van Duyne and J. O. Smith III, "Physical modeling with the 2-D digital waveguide mesh," in *Proc. Int. Computer Music Conf. (ICMC)*, Tokyo, Japan, 1993.

[11] J. Conway and N. J. A. Sloane, *Sphere packings, lattices and groups*. Springer-Verlag, 1988.

[12] S. Bilbao, "Wave and scattering methods for the numerical integration of partial differential equations," Ph.D. thesis, Stanford University, 2001.

[13] N. W. Ashcroft and N. D. Mermin, *Solid State Physics*. Saunders College, Philadelphia, 1976.

[14] S. A. van Duyne and J. O. Smith III, "The tetrahedral digital waveguide mesh," in *Proc. IEEE WASPAA*, 1995, pp. 234–237.

[15] L. Savioja, "Improving the three-dimensional digital waveguide mesh by interpolation," *Proc. Nordic Acoustical Meeting*, pp. 265–268, 1998.

[16] S. Bilbao, *Numerical sound synthesis: finite difference schemes and simulation in musical acoustics*. Wiley, 2009.

[17] A. Southern, D. T. Murphy, T. Lokki, and L. Savioja, "The perceptual effects of dispersion error on room acoustic model auralization," in *Proc. Forum Acusticum, Aalborg, Denmark*, 2011, pp. 1553–1558.

[18] L. Savioja, "Real-time 3D finite-difference time-domain simulation of low-and mid-frequency room acoustics," in *Proc. Digital Audio Effects (DAFx)*, vol. 1, 2010, p. 75.

[19] C. J. Webb and A. Gray, "Large-scale virtual acoustics simulation at audio rates using three dimensional finite difference time domain and multiple GPUs," in *Proc. Int. Cong. Acoustics (ICA)*, Montréal, Canada, 2013.

[20] S. Bilbao and J. O. Smith III, "Finite difference schemes and digital waveguide networks for the wave equation: Stability, passivity, and numerical dispersion," *IEEE Trans. Speech and Audio Processing*, vol. 11, no. 3, pp. 255–266, 2003.

[21] L. Savioja and V. Välimäki, "Interpolated rectangular 3-D digital waveguide mesh algorithms with frequency warping," *IEEE Trans. Speech and Audio Processing*, vol. 11, no. 6, pp. 783–790, 2003.

[22] G. R. Campos and D. M. Howard, "On the computational efficiency of different waveguide mesh topologies for room acoustic simulation," *IEEE Trans. Speech and Audio Processing*, vol. 13, no. 5, pp. 1063–1072, 2005.

[23] K. Kowalczyk and M. van Walstijn, "Room acoustics simulation using 3-D compact explicit FDTD schemes," *IEEE Trans. Audio, Speech, and Language Processing*, vol. 19, no. 1, pp. 34–46, 2011.

[24] B. Hamilton and S. Bilbao, "Hexagonal vs. rectilinear grids for explicit finite difference schemes for the two-dimensional wave equation," in *Proc. Int. Cong. Acoustics (ICA)*, Montréal, Canada, 2013.

[25] D. P. Petersen and D. Middleton, "Sampling and reconstruction of wave-number-limited functions in N-dimensional Euclidean spaces," *Information and control*, vol. 5, no. 4, pp. 279–323, 1962.

[26] S. Bilbao, "Modeling of complex geometries and boundary conditions in finite difference/finite volume time domain room acoustics simulation," *IEEE Trans. Audio, Speech, and Language Processing*, vol. 21, no. 7, pp. 1524–1533, Jul. 2013.

[27] K. Petkov, F. Qiu, Z. Fan, A. E. Kaufman, and K. Mueller, "Efficient LBM visual simulation on face-centered cubic lattices," *IEEE Trans. Visualization and Computer Graphics*, vol. 15, no. 5, pp. 802–814, 2009.

[28] X. Fei, T. Xiaohong, and Z. Xianjing, "The construction of low-dispersive FDTD on hexagon," *IEEE Trans. Antennas and Propagation*, vol. 53, no. 11, pp. 3697–3703, 2005.

[29] N. Röber, M. Spindler, and M. Masuch, "Waveguide-based room acoustics through graphics hardware," in *Proc. Int. Computer Music Conf. (ICMC)*, 2006.

[30] M. Potter, M. Lamoureux, and M. Nauta, "An FDTD scheme on a face-centered-cubic (FCC) grid for the solution of the wave equation," *J. Computational Physics*, vol. 230, no. 15, pp. 6169–6183, 2011.

[31] L. V. Kantorovich and V. I. Krylov, *Approximate methods of higher analysis. Translated by Curtis D. Benster*. Interscience Publishers, 1958.

[32] J. G. Charney, R. Fjörtoft, and J. von Neumann, "Numerical integration of the barotropic vorticity equation," *Tellus*, vol. 2, no. 4, pp. 237–254, 1950.

[33] Y. Liu, "Fourier analysis of numerical algorithms for the Maxwell equations," *J. Computational Physics*, vol. 124, no. 2, pp. 396–416, 1996.

[34] B. Hamilton and C. J. Webb, "Room acoustics modelling using GPU-accelerated finite difference and finite volume methods on a face-centered cubic grid," in *Proc. Digital Audio Effects (DAFx)*, Maynooth, Ireland, 2013.

[35] M. van Walstijn and K. Kowalczyk, "On the numerical solution of the 2D wave equation with compact FDTD schemes," in *Proc. Digital Audio Effects (DAFx)*, Espoo, Finland, 2008, pp. 205–212.